

Void fraction measurements in partial cavitation regimes by X-ray computed tomography

Jahangir, Saad; Wagner, Evert C.; Mudde, Robert F.; Poelma, Christian

DOI

[10.1016/j.ijmultiphaseflow.2019.103085](https://doi.org/10.1016/j.ijmultiphaseflow.2019.103085)

Publication date

2019

Document Version

Final published version

Published in

International Journal of Multiphase Flow

Citation (APA)

Jahangir, S., Wagner, E. C., Mudde, R. F., & Poelma, C. (2019). Void fraction measurements in partial cavitation regimes by X-ray computed tomography. *International Journal of Multiphase Flow*, 120, Article 103085. <https://doi.org/10.1016/j.ijmultiphaseflow.2019.103085>

Important note

To cite this publication, please use the final published version (if applicable). Please check the document version above.

Copyright

Other than for strictly personal use, it is not permitted to download, forward or distribute the text or part of it, without the consent of the author(s) and/or copyright holder(s), unless the work is under an open content license such as Creative Commons.

Takedown policy

Please contact us and provide details if you believe this document breaches copyrights. We will remove access to the work immediately and investigate your claim.

Green Open Access added to TU Delft Institutional Repository

'You share, we take care!' – Taverne project

<https://www.openaccess.nl/en/you-share-we-take-care>

Otherwise as indicated in the copyright section: the publisher is the copyright holder of this work and the author uses the Dutch legislation to make this work public.



Void fraction measurements in partial cavitation regimes by X-ray computed tomography



Saad Jahangir^a, Evert C. Wagner^b, Robert F. Mudde^b, Christian Poelma^{a,*}

^a Department of Process & Energy (Faculty 3mE), Delft University of Technology, Leeghwaterstraat 21, 2628 CA Delft, The Netherlands

^b Department of Chemical Engineering (Faculty of Applied Sciences), Delft University of Technology, Van der Maasweg 9, 2629 HZ Delft, The Netherlands

ARTICLE INFO

Article history:

Received 29 November 2018

Revised 9 June 2019

Accepted 3 August 2019

Available online 7 August 2019

Keywords:

X-Ray computed tomography

Cavitation

Venturi

Multiphase flow

ABSTRACT

Cavitation is a complicated multiphase phenomenon, where the production of vapor cavities leads to an opaque flow. Exploring the internal structures of the cavitating flows is one of the most significant challenges in this field of study. While it is not possible to visualize the interior of the cavity with visible light, we use X-ray computed tomography to obtain the time-averaged void fraction distribution in an axisymmetric converging-diverging nozzle ('venturi'). This technique is based on the amount of energy absorbed by the material, which in turn depends on its density and thickness. Using this technique, two different partial cavitation mechanisms are examined: the re-entrant jet mechanism and the bubbly shock mechanism. 3D reconstruction of the X-ray images is used (i) to differentiate between vapor and liquid phase, (ii) to obtain radial geometric features of the flow, and (iii) to quantify the local void fraction. The void fraction downstream of the venturi in the bubbly shock mechanism is found to be more than twice compared to the re-entrant jet mechanism. The results show the presence of intense cavitation at the walls of the venturi. Moreover, the vapor phase mixes with the liquid phase downstream of the venturi, resulting in cloud-like cavitation.

© 2019 Elsevier Ltd. All rights reserved.

1. Introduction

Cavitation in a flow occurs when the static pressure in the flow falls below the vapor pressure of the liquid, resulting in the formation of vapor bubbles. In many hydrodynamic applications, such as ship propellers, hydro turbines or diesel injectors, cavitation often cannot be avoided due to their operating conditions. If a cavitation bubble or cloud collapses close enough to a solid wall, it will produce a high-speed micro-jet and shock waves, which can result in erosion (Franc and Michel, 2006; Dular and Petkovič, 2015; Peng et al., 2018). Understanding the correct cavitation physics is important because then the adverse consequences such as erosion can be diminished.

It is of great importance to understand the development and dynamics of local void fractions in cavitating flows. Among the studies on cavitation, high-speed visualization is the most popular technique to investigate the cavitation evolution (Laberteaux et al., 1998; Chen et al., 2015). Simple optical methods are limited to investigating cavitation occurring close to the wall region. However, quantitative information regarding the void fractions is difficult to obtain from high-speed imaging, because the cavitation bubbles

block and scatter light and thus make the flow opaque (Dash et al., 2018). Due to the lack of penetrability of visible light in such optically opaque flows, advanced alternative techniques have been developed over the years to quantitatively characterize the phenomena occurring in the interior of the flow and to quantify void fractions. Broadly, these techniques include optical probes, Electrical Capacitance Tomography, Radioactive Particle Tracking, (X-ray/Gamma ray) Computed Tomography (CT), Magnetic Resonance Imaging, with each technique having its advantages and limitations. Quantitative non-intrusive techniques have been reviewed in literature (Chaouki et al., 1997; Kastengren and Powell, 2014). Impedance tomography systems have been developed to investigate multiphase flows, and they are reviewed by Holder (2004). Impedance tomography systems are relatively cheap, but such systems are limited by the number of electrodes that can be located on the boundary. This limits the spatial resolution that can be achieved in the reconstruction. Gamma and X-ray imaging have been used to study multiphase flows such as cavitating flows and bubbly flows. X-ray imaging has been demonstrated as a valuable technique to quantify the void fractions in various cavitation related studies (Bauer et al., 2012; Mäkiharju et al., 2013; Mitroglou et al., 2016; Khelifa et al., 2017). Void fractions are of high importance for the understanding of shedding behavior in periodic cavitation. Recently Ganesh et al. (2016) found that under particular

* Corresponding author.

E-mail address: C.Poelma@tudelft.nl (C. Poelma).

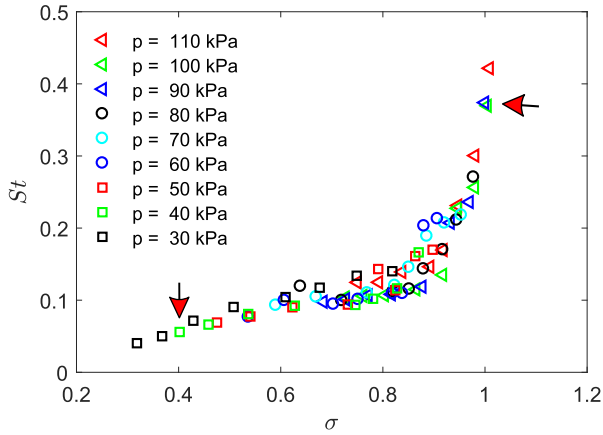


Fig. 1. Dimensionless frequency of the cavitation shedding cycle as a function of the cavitation number for the venturi, replotted from Jahangir et al. (2018). The red arrows show the cavitation numbers selected for the CT reconstruction. (For interpretation of the references to colour in this figure legend, the reader is referred to the web version of this article.)

conditions a condensation shock can be the dominant mechanism for periodic cavitation shedding, instead of the re-entrant jet. Time-resolved X-ray densitometry was used to investigate the local void fractions in the flow field. They found that void fractions increase with an increase in cavitation intensity. These experiments were performed on a 2D wedge. A converging-diverging nozzle ('venturi') is used in this study. Due to its high contraction ratio, a broader cavitation dynamic range can be attained. However, by using a standard 2D X-ray densitometry system, only information integrated along lines of sight about the void fraction within the region of interest can be determined from a single viewing angle. It is unlikely to obtain information regarding the structures inside the cavitation.

X-ray CT is widely used in medical imaging. It uses the relation between the material properties and the attenuation coefficient of X-rays. Images are created using the attenuation along the beam paths recorded at various viewing angles. This capability inspired the idea to use X-ray CT to measure the void fraction distribution and radial geometric characteristics in the flow. Bauer et al. (2012) did the first study to investigate an internal cavitation flow with the X-ray CT-scanner on a purpose-built nozzle. Mitroglou et al. (2016) also performed X-ray CT measurements on a smaller scale nozzle ($D = 3$ mm). From both of these studies, the obtained time-averaged CT images gave useful insights on the flow structures inside the nozzle. However, all the previous studies which investigated the internal cavitation flow were performed on nozzles, to the best of authors knowledge. Using a nozzle with a constant diameter, it is impossible to obtain different partial cavitation regimes.

Jahangir et al. (2018) used a venturi in combination with high-speed visualization to distinguish between two partial cavitation regimes: the re-entrant jet mechanism and the bubbly shock mechanism. The authors further showed that the non-dimensional frequency (Strouhal number) can be used to identify the two partial cavitation regimes. The Strouhal number (St) is defined as:

$$St = \frac{fD_0}{u_0}, \quad (1)$$

where D_0 is the throat diameter, the shedding frequency of the cavitation clouds is given by f and u_0 is the free stream velocity of the flow in the venturi throat. In Fig. 1, the Strouhal number (St) is shown as a function of the cavitation number. The cavita-

tion number (σ) is defined as:

$$\sigma = \frac{p - p_v}{\frac{1}{2}\rho u_0^2}, \quad (2)$$

where p is the downstream pressure, p_v is the vapor pressure¹ of the liquid at the temperature of the setup and ρ is the density of the fluid. The shedding frequency was determined using high-speed shadowgraphy. Details can be found in Jahangir et al. (2018). The study found that all points collapsed on a single curve, with the shedding frequency being a function of cavitation number. From visual inspection of the shadowgraphy data taken for various cases in Fig. 1, two different cavitation mechanisms were identified as a function of cavitation number: for $\sigma > 0.95$ cloud cavitation shedding is governed by the re-entrant jet mechanism. For $\sigma < 0.75$ cloud cavitation shedding is governed by the bubbly shock mechanism. The cavitation region in between is governed by both mechanisms, so it is called the transition region. In this study, we will examine the void fractions using X-ray CT in the above-mentioned regimes using the same geometry (see also Fig. 2, discussed in detail later). To that end, one of the representative case from both the re-entrant jet mechanism and the bubbly shock mechanism will be used for the determination of void fractions. A case with the cavitation number of $\sigma = 1$ from the re-entrant jet mechanism is selected and another case with $\sigma = 0.40$ from the bubbly shock mechanism is selected (shown with red arrows in Fig. 1).

The advantage of the X-ray CT is that it does not only measure the spatial average of the void fraction like it would be for standard X-ray imaging, but the void fraction distribution along different cross-sections of the venturi. The data is essential to validate our assumptions regarding the physical mechanisms. Furthermore, it is currently being used to validate numerical models.

The manuscript is organized in the following manner. The experimental details are described in Section 2, while Section 3 explains in detail the data processing and methods used to explain the flow dynamics. The calibration and results are reported in Section 4. The conclusions follow in Section 5.

2. Experimental details

2.1. Flow facility

A schematic overview of the flow setup utilized for the experiments is represented in Fig. 2. The flow in the closed-loop system is driven by a centrifugal pump, and a flowmeter (KROHNE flowmeter, type: IFS 4000F/6) is used to measure the volumetric flow rate (Q). The measurements from the downstream pressure transducer (calculated from P_3 in Fig. 2), the flowmeter, and the temperature sensor are used to determine the cavitation number. A water column present at an angle (due to space constraints) is used to collect the air bubbles entrained in the flow during degasification, and to vary the global static pressure of the system. A vacuum pump is used to control the global static pressure below ambient pressure down to 20 kPa absolute. The experimental setup shown in Fig. 2 had to be reoriented for the X-ray imaging measurements compared to shadowgraphy measurements performed by Jahangir et al. (2018) due to space restrictions of the X-ray facility. Therefore, the entrance length had to be reduced from 40D to 10D. Nevertheless, the flows from the two experiments for the same cavitation number were confirmed to be equivalent, as the pressure loss coefficients across the venturi (K) were alike for both cases (explained in Section 4). The pressure loss coefficient K

¹ The vapor pressure is calculated using the Antoine equation at the temperature measured during the experiments (18 °C - 26 °C).

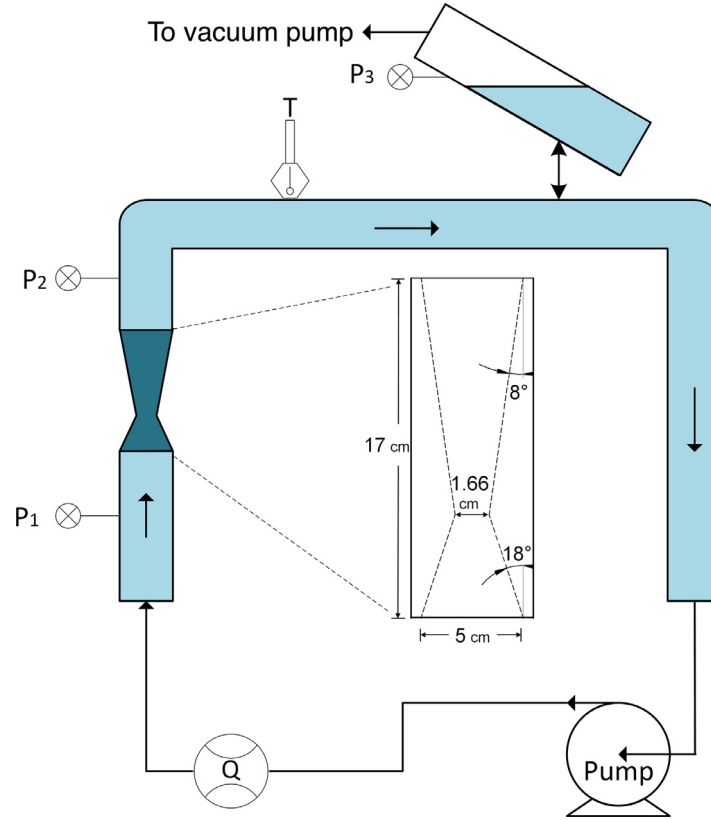


Fig. 2. Schematic overview of the experimental facility indicating essential components (dimensions not to scale). The inset shows the geometry and relevant dimensions of the converging-diverging section.

is given by:

$$K = \frac{\Delta p}{\frac{1}{2}\rho u_0^2}, \quad (3)$$

where Δp is the pressure loss over the venturi (calculated from P_1 and P_2 in Fig. 2). A visual examination also established symmetry of the top and bottom halves of the time-averaged shadowgraphy images by placing a mirror at an angle of 45° below the venturi in the horizontal configuration. The side-view and the bottom-view were visualized simultaneously, in order to verify whether the cavitation dynamics are axisymmetric. No significant difference was found, therefore effects due to gravity can be neglected.

In Fig. 2(inset), a picture of the venturi can be seen with its geometrical parameters. The venturi is milled out from a block of polymethylmethacrylate (PMMA) and has a throat diameter (D_0) of 16.67 mm. The convergence and divergence angles are 18° and 8° to the axis, respectively (inspired by previous studies: Long et al. (2017), Hayashi and Sato (2014), and Tomov et al. (2016)). An area ratio of 1:9 (area of the throat versus exit area) is chosen. The flow direction is from bottom to top in the venturi. Further details on the experimental setup can be found in Jahangir et al. (2018).

2.2. Experimental procedure

A vacuum pump is utilized to degasify the water before the experiments. A water sample is taken for the determination of the gas content in the system using an oxygen sensor (RDO PRO-X Probe). After running the setup for 60 minutes at lower ambient pressure with cavitation, the oxygen content reduces from oversaturated to approximately 40%. All the measurements were performed at approximately the same oxygen content.

The setup is run for 5 minutes before the measurement series is started, in order to mix the water in the system and to obtain a uniform water temperature. The global static pressure of the system is fixed at a prescribed value. The measurements are started when the pressure readings are constant. For the specified global static pressure, measurements are conducted at different flow velocities. A data acquisition system is used to record all the sensor values (pressure, flow rate, and temperature). X-ray images (explained in the upcoming paragraph) are recorded simultaneously. In the end, the oxygen content is measured again by taking a water sample from the setup.

2.3. X-ray imaging

In this study, the cavitating flow inside the venturi was measured using X-ray imaging. The X-ray setup originally consisted of three standard industrial type X-ray sources (Yxlon International GmbH) with a maximum energy of 150 keV working in cone beam mode. Each X-ray source generates a cone beam that can be detected by a detector plate on the opposite side of each X-ray source. For this study, the experiments were performed with one X-ray source and one detector plate to obtain the projected 2D output signals from the 3D cavitating flow.

Fig. 3 (a) and (b) show a photograph of the measurement section in the X-ray setup and schematic overview of the method, respectively. A source-detector pair is used to measure the attenuation of the X-rays through the cavitating venturi. For the experiments, the venturi is placed (inclination ± 1 mm/m) in the center of the setup and 323 ± 2 mm from the X-ray source and 584 ± 2 mm from the detector plate. The X-ray source (Yxlon-Y.TU 160-D06) has a tungsten anode. The source is operated at 120 keV and 5 mA in order to achieve a high contrast between the liquid

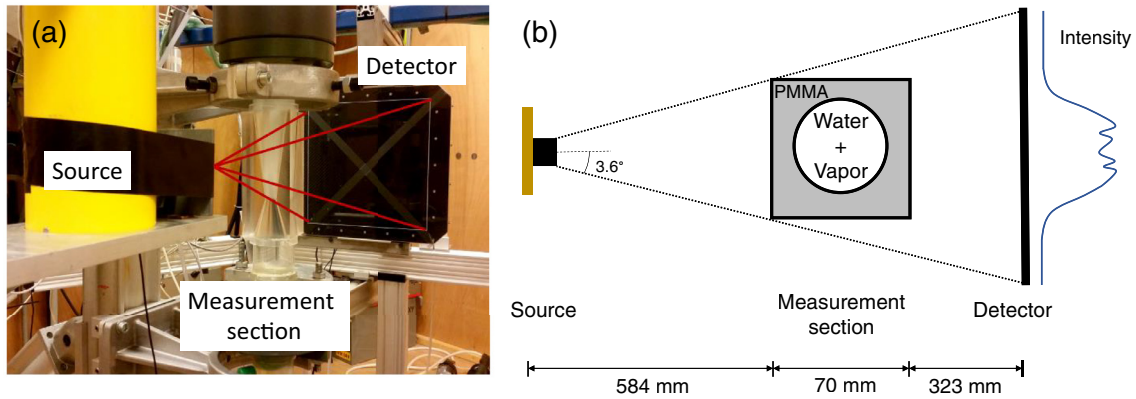


Fig. 3. The basic arrangement and components of the X-ray setup and the flow facility. (a) Test-rig inside the X-ray setup. (b) Schematic of the X-ray imaging method with the source on the left, the measurement section in the middle, and the detector on the right indicating the intensity (dimensions not to scale).

and vapor phases within the venturi. The flat detector, Xineos-3131 CMOS model, consists of a $307 \times 302 \text{ mm}^2$ sensitive area. The detector provides the total photon count in the range of 40–120 keV. For the experiments, a field of view of 1548×660 pixels is chosen. Each pixel has a size of $198 \times 198 \mu\text{m}^2$ with 14 bits of pixel depth.

The entire experimental procedure was controlled with a workstation outside the setup room (closed with a lead sheet) guaranteeing a safe working condition. Using the workstation, it was possible to trigger the X-ray source and read out the signals from the detector plate. Further details on the X-ray setup and the measurement technique can be found in [Mudde et al. \(2008\)](#), [Maurer et al. \(2015\)](#), and [Helmi et al. \(2017\)](#). The X-ray images are recorded at 61 Hz during approximately 1 minute, which corresponds to 3700 images. Afterwards, these images are averaged. All results reported in the present study are based on the time-averaged X-ray images. As the typical shedding frequency is 40 Hz at $\sigma = 0.46$, this ensures that the statistics are based on sufficient shedding cycles.

3. Data processing

3.1. Image processing

The raw images acquired by the X-ray detector need several post-processing steps (black lines correction, background subtraction, and image adjustment) before they can be used to explain the cavitation dynamics. All of the following steps were performed using Matlab R2017a (The Mathworks Inc., Natick, USA) and the process is depicted in [Fig. 4](#). Due to the orientation of venturi in the experimental setup, the images obtained from the X-ray detector show the venturi in a vertical position. The X-ray images were rotated by 90° ; therefore, the bulk flow is from left to right in all images shown in the paper.

The detector plate is constructed by a combination of smaller detector elements. Due to this construction, multiple black lines appear on the obtained images, as shown in [Fig. 4\(a\)](#). These black lines consist of a single pixel in either direction (vertical direction and horizontal direction), and they do not contain any data. These were replaced with intensities by linear interpolation of the pixel intensities on either side of the lines, as shown in [Fig. 4\(b\)](#). In the X-ray images, the vapor phase has higher grayscale intensities, while the liquid phase has lower grayscale intensities. This happens because the presence of vapor leads to lower attenuation of the X-rays along its path length (explained in [Section 4.2](#)). A background correction is performed for the X-ray images, for which background images with only the liquid phase without flow are captured. In order to improve the contrast, an image adjustment

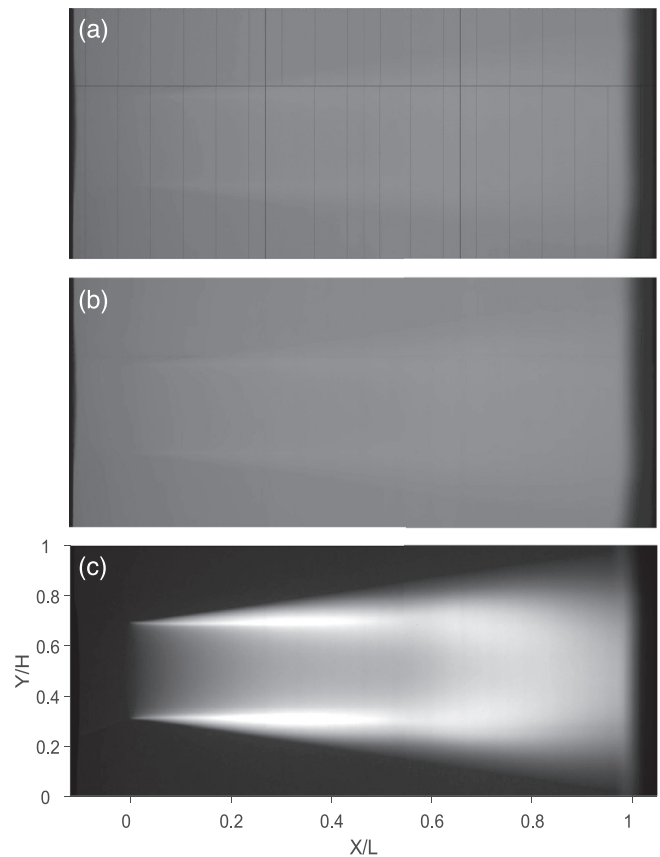


Fig. 4. Time-averaged X-ray images of cavitating flow in the venturi: (a) raw time-averaged image obtained from the detector, (b) corrected image after removing black lines, and (c) the image obtained after background correction as well as adjusted to improve contrast (vapor is light gray, liquid is black). In all the images, the bulk flow occurs from the left to right.

operation is performed on images. This process involves rescaling the grayscale intensities in order to have 1% of the data being saturated at high intensities and 1% of the data covering low intensities ([Fig. 4\(c\)](#)). This arbitrary scaling has no influence on the quantitative void fraction, as this is based on a separate calibration procedure (discussed in [Section 4.2](#)).

As the vertical axis is not used (as will be discussed later), its origin is set arbitrarily. The origin of the horizontal axis, coinciding with the axial/streamwise direction, is set at the throat of the

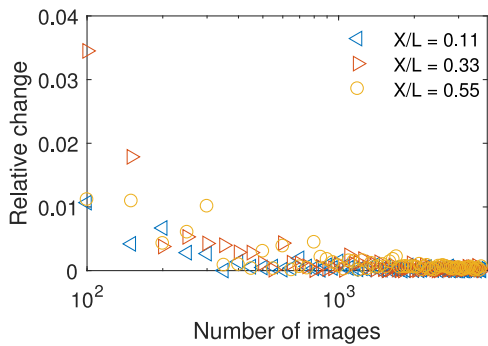


Fig. 5. Convergence study of the time-averaged X-ray images, using three points on the centerline. The relative change is less than 0.1% after 3700 images.

venturi. The axial location (X) is made dimensionless using the length of the measured part of the diverging section ($L = 9.3$ cm).

A convergence study was conducted on the X-ray data of the cavitating flow, as shown in Fig. 5. The term on the y-axis ('relative change') is calculated as follows: three points along the centerline are chosen: $X/L = 0.11$, 0.33 and 0.55 , which cover regions containing cavitation. The averaged grayscale intensities of these points are computed from the first 50 X-ray images. Subsequently, an additional 50 images are used to calculate the new mean intensities. The difference between the new and old mean, divided by the old mean is shown as a function of the amount of total images used. The relative error reduces to less than 0.1% after 3700 images. Hence, the sampling time of one minute allows obtaining sufficient data for statistics with a minimum error from the mean.

3.2. Computed tomography

CT, also known as computed tomography, makes use of computer-processed combinations of many X-ray measurements taken from different angles to produce cross-sectional images

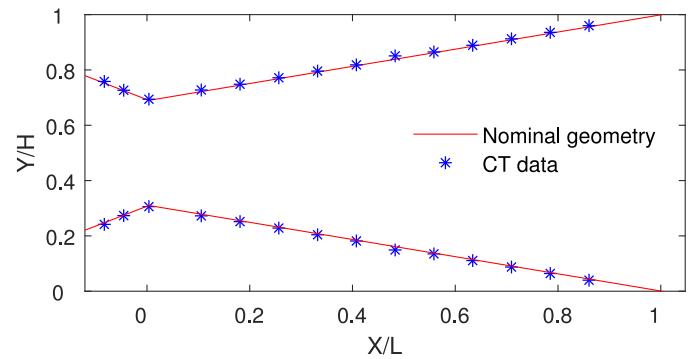


Fig. 7. Validation of the diameters from CT slices using the nominal geometry. See text for details.

('slices'). The process of CT involves a collection of projections from several angles of the X-ray intensity attenuated by the object of interest on the detector. The collected data ('sinogram') is then reconstructed utilizing algorithms, such as filtered back projection.

In the X-ray imaging system used in this study shown in Fig. 3, the distance between the detector and the source is much larger than the measuring area, and the viewing angle is minimal. The difference between the path lengths measured at the maximum angle and parallel to the detector is 0.1% of the parallel beam path. Therefore, the cavitation cloud is assumed to be projected to the detector by parallel X-ray beams (Wang et al., 2018). This assumption is also validated by comparing the reconstructed geometry against the nominal geometry, as shown in Fig. 7 (explained in the upcoming paragraph). As the measurement section is axisymmetric, we assume axisymmetry of the time-averaged flow. Fig. 6(a) shows a time-averaged X-ray image, the starting point for our analysis. The red lines indicate the overall shape of the venturi. Note that we have shifted these lines outward by a few pixels so that they do not obscure the data. For all upcoming figures this minor

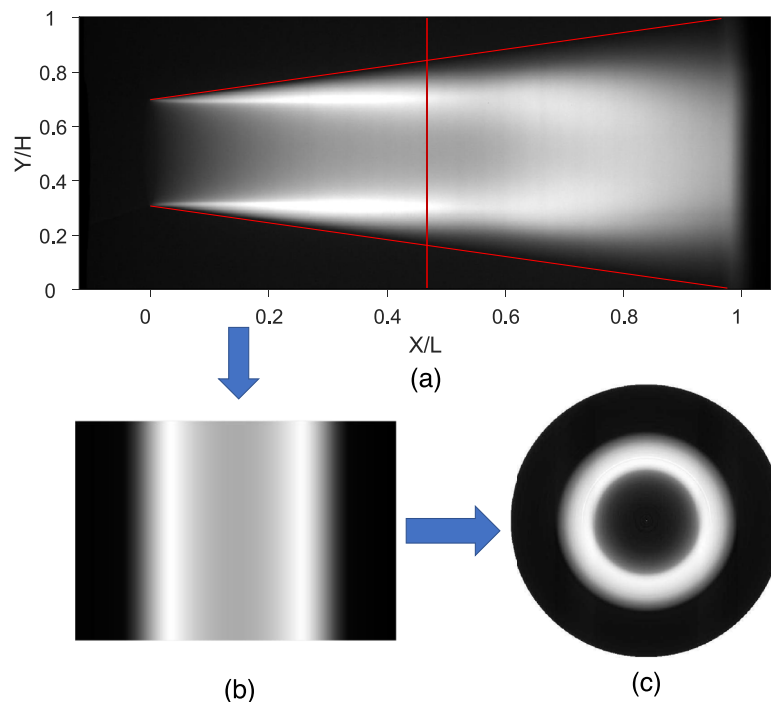


Fig. 6. Schematic of post-processing procedure followed to obtain a cross-sectional CT slice. (a) Time-averaged X-ray image of the cavitating venturi at $\sigma = 0.40$ (vapor is light gray, liquid is black). (b) Sinogram created from an axial location (red line in (a)). (c) Cross-sectional CT image presented as side-view cut. See text for details on this procedure. (For interpretation of the references to colour in this figure legend, the reader is referred to the web version of this article.)

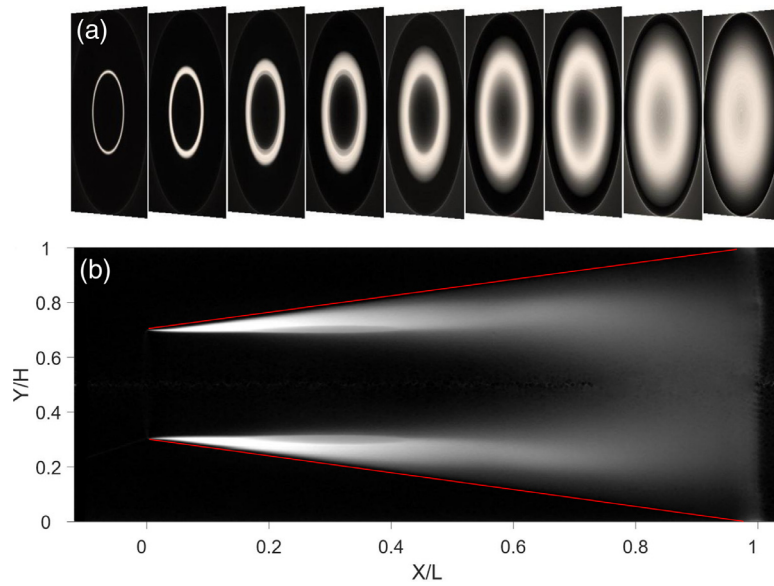


Fig. 8. (a) Cross-sectional CT images at different axial positions showing growth of the cavitation cloud at $\sigma = 0.40$. The contrast in the images is adjusted individually for each slice for clarity. (b) Cross-section through the x - z plane, showing the presence of cavitation bubbles in the center of the liquid core downstream of the venturi.

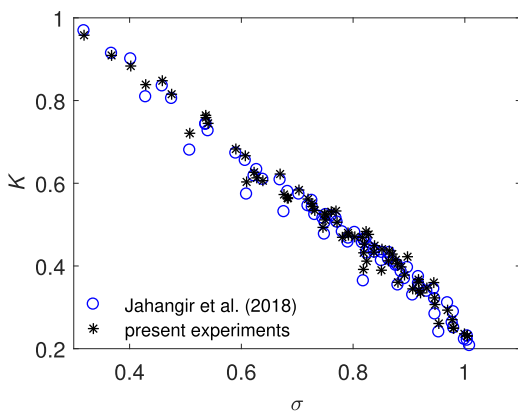


Fig. 9. The pressure loss coefficient (K) as a function of the cavitation number for the experiments performed by [Jahangir et al. \(2018\)](#) (open markers) and the present experiments (asterisks).

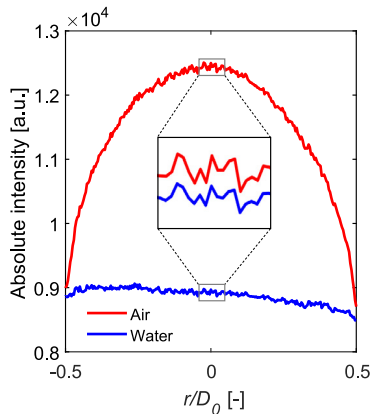


Fig. 10. Profiles of the absolute intensities recorded on the X-ray detectors at one streamwise location: the venturi throat. The two cases considered are when the venturi contains solely air and solely water.

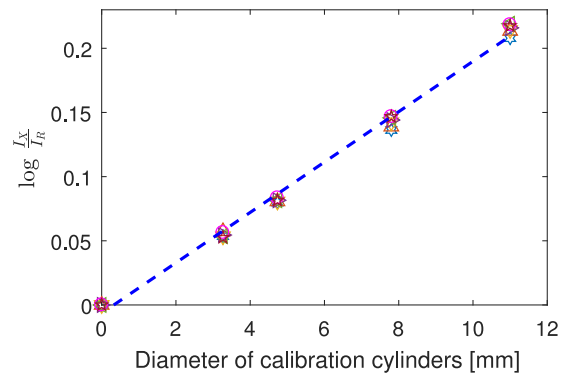


Fig. 11. The logarithm of the ratio of intensities ($\frac{I_x}{I_r}$) versus the diameters of the calibration cylinders representing the actual line-integrated void fractions. The measured grayscale intensity is based on an average of 3700 images.

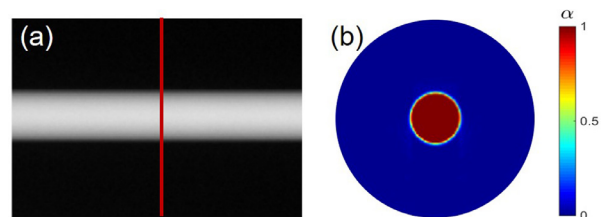


Fig. 12. (a) Time-averaged X-ray image of the calibration cylinder (air is light gray and liquid is black). (b) Cross-sectional CT image presented as a side-view cut with $\alpha = 0.995 \pm 0.004$. The red region indicates the presence of vapor (air in this case) and the blue region indicates the presence of liquid. (For interpretation of the references to colour in this figure legend, the reader is referred to the web version of this article.)

shift was used for clarity. A slice (vertical red line in [Fig. 6\(a\)](#)) is extracted from the time-averaged image and stacked 360 times to construct a sinogram of 600×360 pixels as shown in [Fig. 6\(b\)](#). This sinogram represents the projections from 360° . This is a necessary intermediate step before CT reconstruction using the particular software used here. Filtered back projection is applied to the sinogram using the ASTRA Toolbox v1.8 ([van Aarle et al., 2016](#)). This is a flexible CT reconstruction open source toolbox which uses

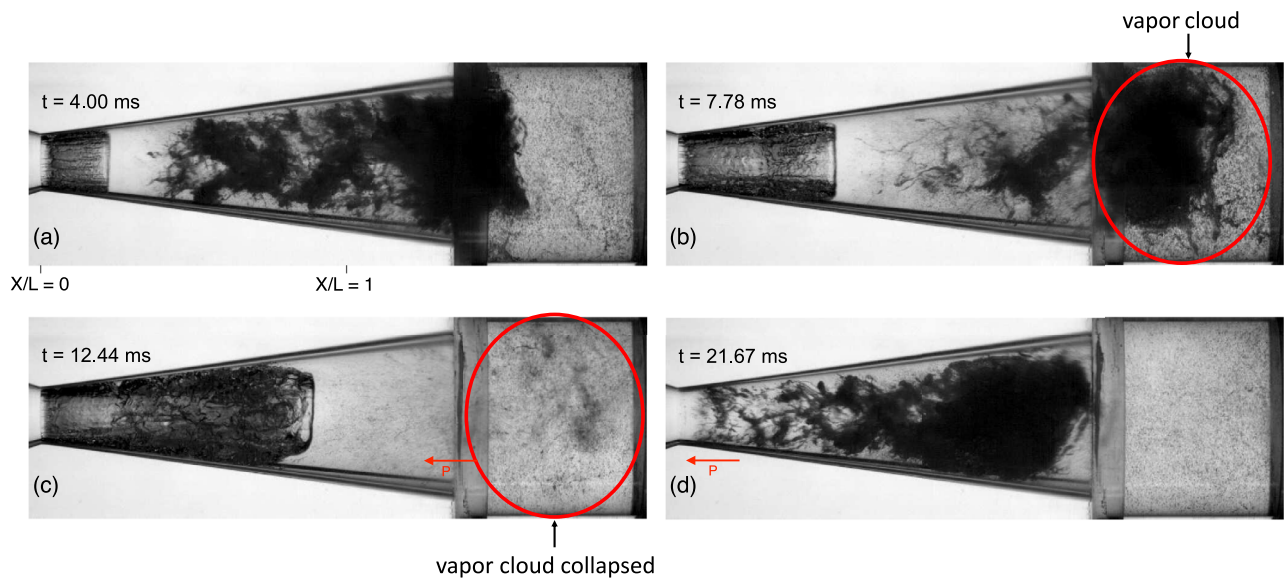


Fig. 13. Video frames of bubbly shock development at $\sigma = 0.40$. The light gray regions indicate the presence of liquid and the dark gray areas indicate the presence of cavity (vapor). (a,b) A growing cavity can be seen (left side of sub-panels) with the previously shed cavity (right side of sub-panels). (c) In the subsequent frame the cavity collapses and a pressure wave is emitted (P). (d) Cavity detachment can be observed when the pressure wave reaches the throat.

CPU and GPU based reconstruction algorithms for 2D and 3D data sets. In the present study, we use a CPU based implementation of the filtered back projection (FBP) algorithm for 2D data sets. It takes the source and detector data as input and returns the reconstruction. For this study, just the sinogram was used as an input and reconstructed CT slice was returned (Fig. 6(c)). The reconstruction algorithm resembles the inverse operation of a forward projection. But instead of each detector getting the line integral of the object function, each point on the object domain receives the value of the detector point where it projects to. So, in essence, the detective function is smeared out over the object domain. This is then done over all projection angles summing up the values in each direction (van Aarle et al., 2016).

A common cause of errors when reconstructing X-ray CT image are artifacts within the image. Conventional sources of artifacts are beam hardening and abrupt changes in density. Beam hardening is the most common artifact found in X-ray CT reconstruction. It causes the edges of the scanned measurement section to appear brighter than the center, even for homogeneous materials (Ketcham and Carlson, 2001). This effect is caused by the difference in absorption coefficients for various wavelengths when using a non-monochromatic source. An efficient way to decrease beam hardening (which is more severe in metals than plastics) is filtering low-energy soft X-rays with metal filters. For these measurements, no beam hardening filtration was used primarily due to the absence of metals which would result in a potential reduction in the image contrast imposed by extra filtration. The absence of beam hardening is also confirmed from the calibration plot, explained in Section 4.2.

Two different tests were performed to check the quality of reconstruction. A check on the diameters from reconstructed CT slices across 14 different axial positions of the full length of empty venturi was performed. The results were compared to the nominal diameters, as shown in Fig. 7. The diameters from CT slices matched quite well to the nominal geometry, a maximum error of less than 1.2% of the local diameter was found. Another check was based on the distribution of void fractions α . The relative error was found to be less than 0.9%, as will be discussed in Section 4.2.

After constructing a single slice, the process is repeated and multiple density slices of the venturi perpendicular to the center-

line axis are created. Fig. 8(a) shows reconstructed slices at different axial positions, showing growth of the cavitation cloud. Most of the vapor is attached to the nozzle wall and persists until four diameters downstream of the throat. This is the point where the cavity detaches during the periodic shedding, which is also confirmed by the high-speed images (Jahangir et al., 2018). After detaching, the vapor cloud moves towards the center of the venturi and mixes with the liquid core. Fig. 8(b) shows the cross-section through the x-z plane. Fig. 8(b) is the cross-section, and thus distinct from the X-ray image of Fig. 7(a). As can be seen in the figure, cavitation bubbles are also present in the liquid core, downstream of the venturi.

4. Results

With the venturi specified in Section 2, it is possible to initiate partial cavitation mechanisms such as the re-entrant jet mechanism and the bubbly shock mechanism at different cavitation numbers. An overview of these cavitation mechanisms can be found in Jahangir et al. (2018).

4.1. Pressure loss coefficient

The strength of cavitation is expressed using the cavitation number. With an increase in the flow velocity, the cavitation number decreases, implying more cavitation. With a decreasing cavitation number, the effective throat diameter is narrowed by the presence of the growing cavity. Because of the narrowed throat diameter for decreasing cavitation number, the pressure loss over the venturi will be higher. This is visible from measurement results, shown in Fig. 9. Here, the cavitation number is varied by changing the flow velocity at different static pressures, and the pressure loss coefficient K is reported. This implies that flow blockage is a function of cavitation number. For both the shadowgraphy experiments performed by Jahangir et al. (2018) and the present X-ray experiments, it can be seen that all points collapse on one line. The flows from the two experiments for the same cavitation numbers are therefore assumed to be equivalent, as the pressure loss coefficients across the venturi (K) are similar for both cases.

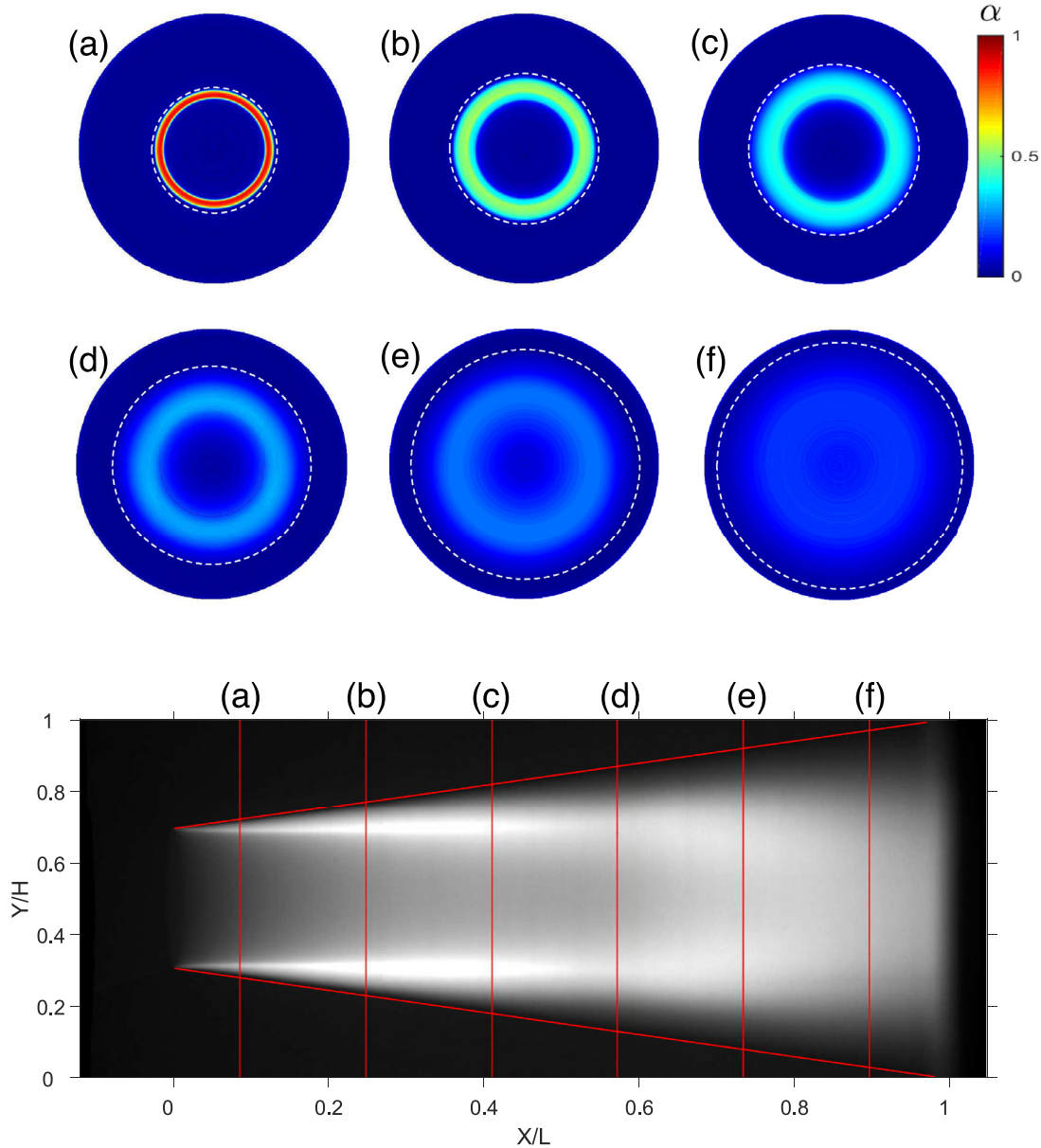


Fig. 14. (Bottom) Time-averaged X-ray image of an experiment in the bubbly shock regime. The light gray regions indicate the presence of vapor and the black regions indicate the presence of liquid. The cavitation number is $\sigma = 0.40$ ($u_0 = 13.7$ m/s and $p = 40$ kPa). (a-f) Quantitative measurements of time-averaged void fractions at six different locations along the venturi.

4.2. CT void fraction calibration

Various approaches exist to obtain quantitative values of the local attenuation coefficient (or density, for simplicity). In our case, we opted for the following approach: images are recorded and divided by a reference image (I_R) for the case of only water. The ‘intensity’ that remains is proportional to the amount of vapor present between source and detector, as this has a lower attenuation than water. Using this reference method, all attenuation outside the region of interest (such as the non-axisymmetric PMMA parts of the test section) cancels out. The images are processed using the CT algorithm, which provides a three-dimensional reconstruction. Each voxel in this reconstruction contains information about the local attenuation coefficient. As our approach is based on relative X-ray image intensities, there is an unknown constant linking voxel values and the actual local attenuation. This coefficient is obtained from calibration experiments.

First, intensities were measured by the X-ray detector when the venturi contained only air and only water. Densities of air (1.27 kg/m³) and water vapor² (0.804 kg/m³) are far smaller than the density of water (997 kg/m³). Therefore, air is a suitable alternative for water vapor because of the negligible difference in their mass densities and hence similar linear absorption coefficients (Mitroglou et al., 2016; Bauer et al., 2018). For the calibration with air, the venturi was left empty and it was filled with filtered water for the other case. The maximum intensity was recorded as 12,580 for air, and it was 9045 for water at the streamwise plane of the throat, as shown in Fig. 10. Approximately 21% of the total capacity of the 14-bit detector was utilized here. However, this range increases in the downstream direction with the increasing

² The reported value for water vapor is at standard conditions. In reality, the pressure (and density) will be lower, but this difference is negligible compared to the difference between water vapor and water.

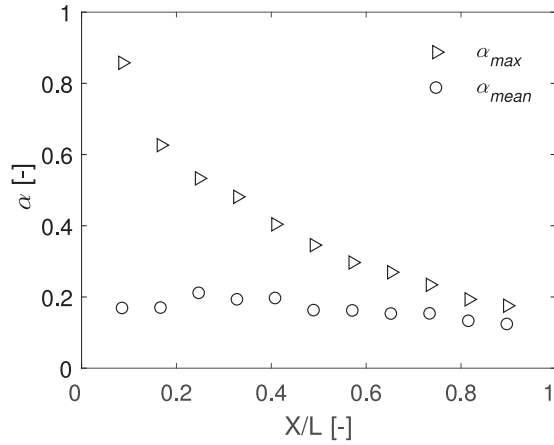


Fig. 15. Time-averaged mean and maximum void fractions of vapor as a function of position for $\sigma = 0.40$.

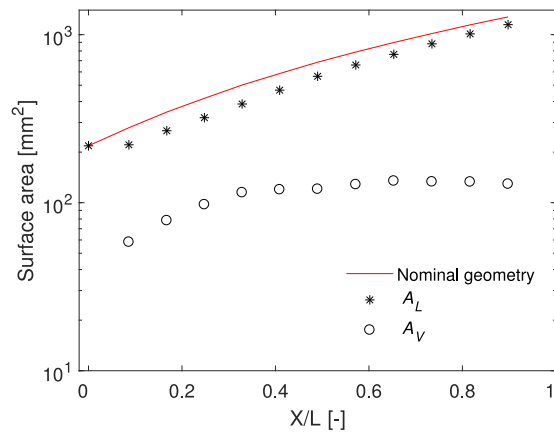


Fig. 16. The total area covered by vapor (A_V) and liquid (A_L) as a function of position for $\sigma = 0.40$. Also shown is the local cross-sectional area of the venturi geometry.

diameter of the venturi cross-section. The wiggles in the absolute intensities (Fig. 10(inset)) are due to different sensitivities of multiple pixels in the primary detector (described in Section 3.1) and not random noise.

For purely monochromatic X-rays, this two-point calibration would have been sufficient to determine all possible values in between vapor/air and water. To ensure accurate results for our X-ray source, additional calibration experiments were performed with increasing volume fractions in between the two extremes. An additional reason is that the expected void fractions are low, so we would be close to one of the calibration points, making the result very sensitive to calibration errors. To perform these additional calibration experiments, empty calibration cylinders (air-filled plastic cylinders) of four different diameters and negligible wall thicknesses were inserted into the venturi, which was filled with water. The calibration cylinders were aligned with the axis of symmetry of the venturi. The diameters of calibration cylinders were measured with an accuracy of ± 0.5 mm. Calibration was then performed at multiple streamwise locations by recording the mean intensity along the centerline of the cylinders. As the diameters of the calibration cylinders were known, the intensity at the center of the cylinder is related to the line-integrated void fraction. In Fig. 11, the calibration relation is shown for seven X/L locations selected from the full length of the venturi. The diameter of the venturi increases with increasing X/L, which corresponds to the different attenuation of X-rays due to the presence of more wa-

ter and less PMMA. However, by dividing the recorded intensity by the reference intensity this effect of different attenuation cancels out. A linear fit through mean can be seen in the Fig. 11. The standard error from the mean for the measured intensities for the various calibration cylinders was found to be less than 3.65%, which is considered acceptable. The relationship obtained between the logarithm³ of the intensities in the X-ray images and the diameter of calibration cylinders (known void fraction) is used to determine the calibration constant, which is then used to calculate the vapor distribution on the reconstructed CT slices (explained in the upcoming paragraph).

To use these calibration results of line-integrated quantities for our CT results, a procedure was followed that is a common method in the X-ray community (selectively Mitroglou et al., 2016; Duke et al., 2015; Bauer et al., 2018). The images from the CT reconstruction provide 3D information. To find the void fraction for each voxel, we collapse the data back to 2D X-ray images, i.e. projecting the tomographic reconstruction onto a 2D plane. We can then assign an integrated void fraction to each projected intensity using the calibration curve. This integrated void fraction is subsequently redistributed over the constructed slice, so that the sum of the voxel values matches the projected void fraction.

Fig. 12 (a) shows the time-averaged X-ray intensity data for a calibration cylinder. This panel is before tomographic reconstruction i.e. a projection along the line between source and detector. Fig. 12(b) shows the reconstructed CT slice at an axial position (red line in Fig. 12(a)) with the void fractions. A very homogeneous distribution of air can be seen. Here, $\alpha = 0.995 \pm 0.004$, which shows a maximum error of approximately 0.9% with respect to real void fraction, which is considered acceptable. This error is associated with various facts, the most notable being: the reconstruction method, which is an approximate approach, and the variation of noise in the X-ray images. The diameter of the cylinder measured from the CT slice also compares very well to the known diameter of the cylinder with an error of less than 1%.

4.3. Cross-sectional distribution of void fraction

This section presents the quantitative void fraction measurements for the bubbly shock mechanism and the re-entrant jet mechanism. The results shown are a mix of qualitative high-speed shadowgraphy images and quantitative time-averaged X-ray measurements. Their combination will assist in interpreting the flow behavior in the venturi.

High-speed shadowgraphy was performed in a prior study, which also provides all relevant technical details (Jahangir et al., 2018). A bright, uniform illumination source is placed behind the venturi and a CMOS camera is used to capture images. Vapor bubbles will block light and thus appear as dark spots in the image. This way the presence and position of vapor cavities can be determined. A framerate of 9000 Hz is used in combination with an exposure time of 1/9000 Hz.

In Fig. 13, video frames of the bubbly shock mechanism are presented. The flow direction is from left to right. The light gray regions indicate the presence of liquid and the dark gray areas indicate the presence of cavity (vapor). A case with cavitation number of $\sigma = 0.40$ ($u_0 = 13.7$ m/s and $p = 40$ kPa) is shown. In Fig. 13(a) and (b), a growing cavity can be seen (left side of sub-panels) with the previously shedded cavity (right side of sub-panels). In the subsequent frame, the cavity collapses and emits a pressure wave. When the pressure wave reaches the venturi throat, the cavity

³ As the intensity decays exponentially in a given medium (cf. the Lambert-Beer law), taking the logarithm of the intensity leads to a linear relation between attenuation (and intensity) and the void fraction.

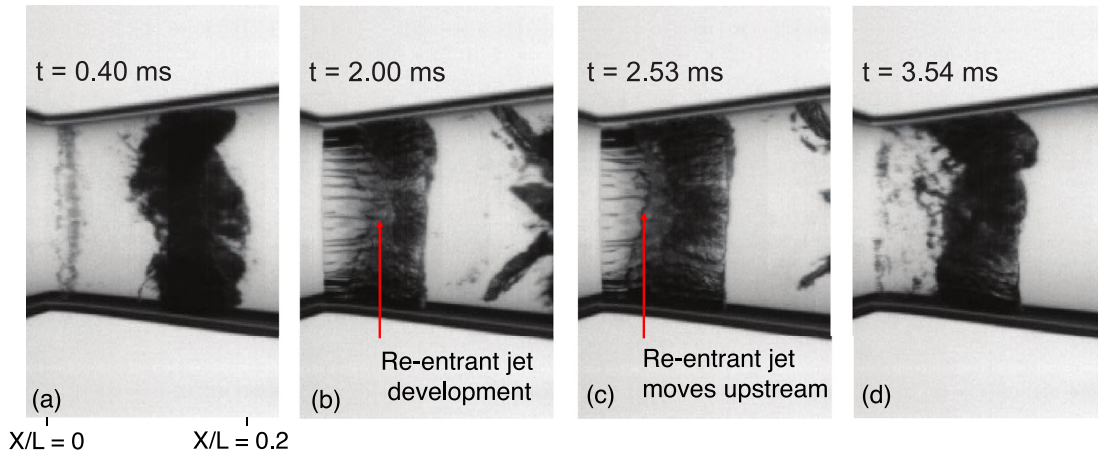


Fig. 17. Video frames of re-entrant jet development at $\sigma = 1$. In (a) and (b), cavity development can be seen and the re-entrant jet starts to develop. The jet front can be recognized by the chaotic interface, which can be seen by the arrow. The propagation of the jet front towards the venturi throat can be seen in (c). In the end, cavity detachment is caused by the re-entrant jet as can be observed in (d).

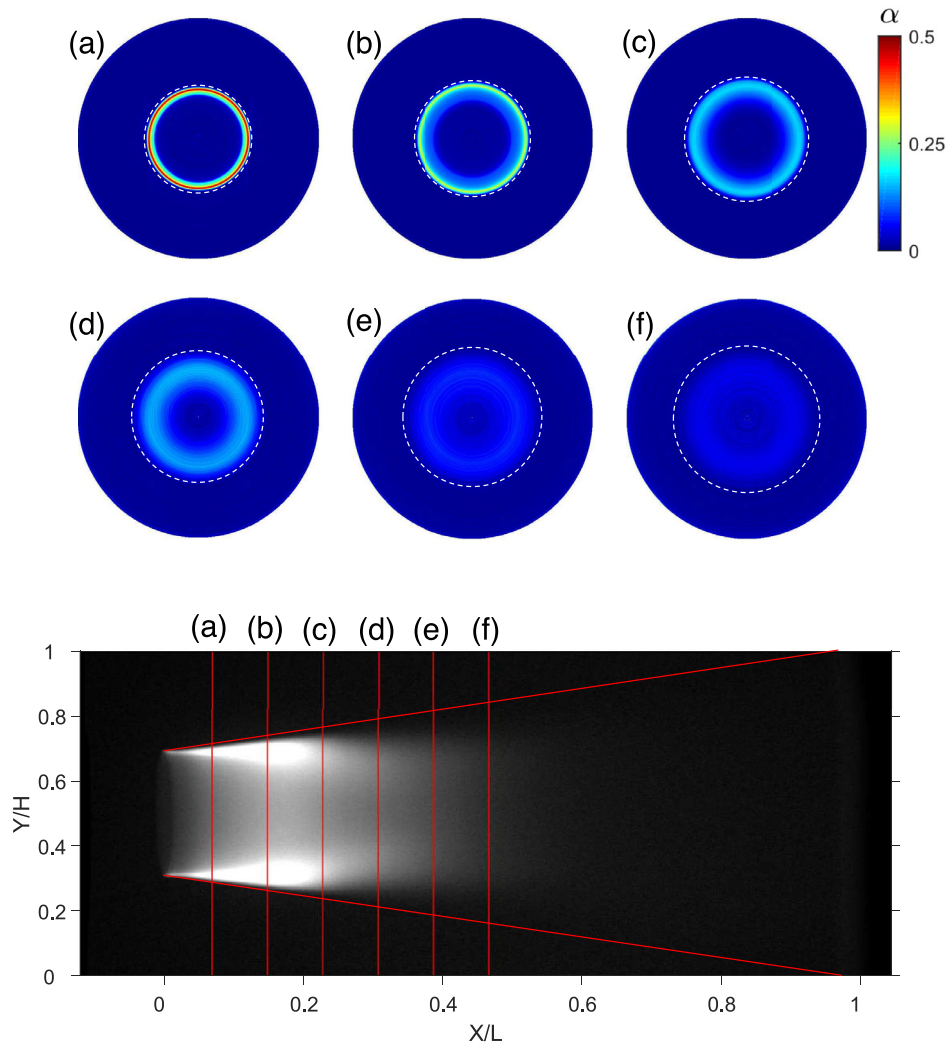


Fig. 18. (Bottom) Time-averaged X-ray image of an experiment in the re-entrant jet regime. The light gray regions indicate the presence of vapor and the black regions indicate the presence of liquid. For this case $\sigma = 1$ (corresponding to: $u_0 = 13.5$ m/s and $p = 90$ kPa). (a-f) Quantitative measurements of time-averaged void fractions at six different locations along the venturi. Note the difference in the color scale compared to Fig. 14.

detaches, as shown in Fig. 13(d). This is the start of the next cycle of the periodic shedding process.

The corresponding void fraction distribution slices for the bubbly shock mechanism are shown in Fig. 14(a) - (f). The CT slices are reconstructed at the axial positions indicated in the time-averaged X-ray image. The flow direction is from left to right. The light gray regions indicate the presence of a cavity (vapor) and the black areas indicate the presence of liquid in the X-ray image, while the red regions show cavity and blue regions show the presence of liquid in the CT slices. Quantitative measures for the total surface area of vapor and liquid A_V and A_L are also obtained for each CT slice. The total surface area of vapor for each CT slice is given by $A_V = \iint \alpha(y, z) dy dz \approx [\Sigma \Sigma \alpha(y, z)] dy dz$, where dy and dz are the physical dimensions of a reconstructed voxel. A_L follows from the nominal local cross-sectional area of the venturi, minus the area covered by vapor.

A core of liquid can be seen in a short distance just downstream of the venturi throat with a concentrated ring of cavitation around it (Fig. 14(a)). This thin film of cavitation has the maximum void fraction of $\alpha_{max} = 0.86$. The center of annulus consists of pure liquid without any cavitation (threshold of liquid being set at $\alpha = 0.016$, explained in Section 4.2). Further downstream of the venturi throat, the vapor film starts to become more like a cloud as its thickness increases, as shown in Fig. 14(b) and (c). A decrease in the maximum void fraction can be seen; however, the average void fraction is similar in both CT slices (Fig. 15).

The cavitation bubbles are present in the liquid core further downstream, hinting at the appearance of a thick cloud of vapor, as shown in Fig. 14(d) and (e). A diffused interface between the liquid and vapor can be also be seen. The vapor film which was previously attached to the circumferential wall can now be seen turning into a cloud and detaching from the wall (Fig. 14(e)). The value of α_{max} steadily decreases with increasing X/L . The cavitation cloud becomes thicker as the liquid core decreases. Note that these are time-averaged void fractions. This is relevant, in particular further downstream, as the cavitation is not present at each instance for a given location: it alternates between liquid and vapor (Fig. 13). The instantaneous void fractions will likely be much higher than the time-averaged data reported here.

In Fig. 14(f), it can be seen that only cloud cavitation appears at the exit of the venturi. The maximum void fractions (α_{max}), the mean void fractions (α_{mean}) and the total surface areas (A_V and A_L) are shown in Figs. 15 and 16. The value of A_V rapidly increases with the increase in axial location until $X/L \approx 0.65$. Here, a maximum of A_V is found of 134.7 mm^2 . With a further increase in X/L , a slight decrease in A_V can be seen. At $X/L = 0.9$, the value of A_V is 129 mm^2 , vapor and liquid are thoroughly mixed with an average void fraction of about 12% and a maximum void fraction of about 16%.

We should not ignore the fact that some part of these void fractions may be attributed to non-condensable gas, instead of just water vapor. The diffusion rate into the cavity is related to the dissolved gas content, the local cavity pressure, and the flow within and around the cavity (Lee et al., 2016). However, to minimize this effect, the measurements were performed at relatively low dissolved gas content (described in Section 2.2).

A second case is selected, but this time in the re-entrant jet dominant regime. The video frames for $\sigma = 1$ ($u_0 = 13.5 \text{ m/s}$ and $p = 90 \text{ kPa}$) are shown in Fig. 17. One full cycle of the re-entrant jet mechanism and shedding can be observed. The re-entrant jet develops with the growing cavity (Fig. 17(a) and (b)). The re-entrant jet front can be recognized by the chaotic interface, which can be seen by the arrow. Then the jet front starts to propagate in the direction of the venturi throat, as shown in Fig. 17(c).

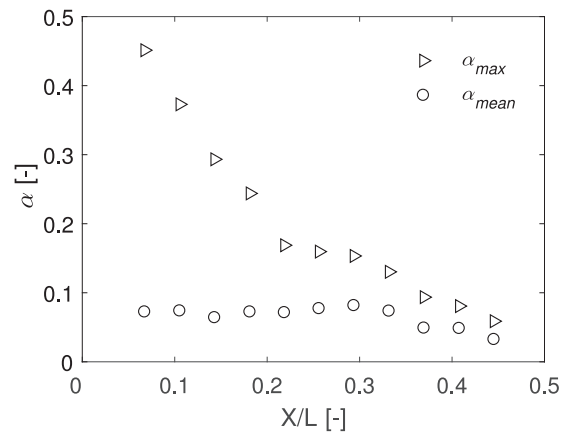


Fig. 19. Time-averaged mean and maximum void fractions of vapor as a function of position for $\sigma = 1$.

The re-entrant jet reaches the throat and the entire cavity detaches from the throat (Fig. 17(d)). This marks the start of the next cycle.

The corresponding void fraction distribution slices for the re-entrant jet mechanism are shown in Fig. 18(a) - (f). Note the difference in color scale compared to Fig. 14. The CT slices are similarly reconstructed at the axial positions indicated in the time-averaged X-ray image. It is evident from the X-ray image that the cavity length is smaller as compared to the bubbly shock case. Therefore, the axial locations for the CT reconstruction are selected accordingly.

One thing that is clearly visible within the CT slices is that the α values for this regime are smaller than those in the bubbly shock governed regime. Once again the core consisting of liquid can be seen in a short distance just downstream of the venturi throat (Fig. 18(a)). The cavitation ring at the circumferential wall is still present; however, its void fraction is less pronounced, compared to Fig. 14. Here, the maximum void fraction is 45%, which is approximately half the void fraction of the bubbly shock governed case. It can also be seen that the extent of the cavitation structure is slightly growing from Fig. 18(a) to (c) but its shape is overall conserved. A decrease in the α_{max} can be seen downstream of the venturi throat (Fig. 18(b)-(d)). However, the average void fraction does not decrease within these three CT slices. In Fig. 18(e) and (f), the cavitation ring changes into cloud cavitation before it vanishes. This proves once more the capabilities of this measurement method.

The maximum and mean void fractions and the total surface areas are shown in Figs. 19 and 20. A_V is the same as the difference between A_L and the nominal local cross-section area, representing the flow blockage caused by cavitation. It is clear that the flow blockage caused by the bubbly shock regime (Fig. 16) is more significant compared to the re-entrant jet regime (Fig. 20). This agrees with the observed difference in pressure drop, see the values of K in the inset of Fig. 9. An increase in A_V can be seen until $X/L \approx 0.3$. Here, $A_V = 33.7 \text{ mm}^2$. The maximum value of A_V is found to be approximately 4 times smaller than the maximum value of A_V in the bubbly shock case. This is a major new insight, as the high-speed shadowgraphy showed fairly similar (time-averaged) data. The value of A_V starts to decrease sharply as we move further downstream and reaches 17.8 mm^2 at $X/L = 0.45$. Here, the maximum void fraction is found to be 6% (Fig. 18(f)), which is quite low as compared to the bubbly shock case. It also hints at the presence of a lower void fraction downstream of the venturi in the re-entrant jet regime as compared to the bubbly shock regime.

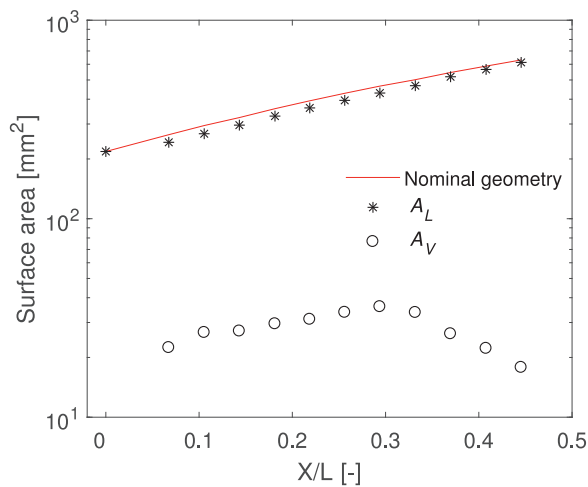


Fig. 20. The total area covered by vapor (A_V) and liquid (A_L) as a function of position for $\sigma = 1$. Also shown is the local cross-sectional area of the venturi geometry.

5. Conclusions and outlook

In this study, the phenomenon of cavitation was examined by CT measurements of the flow through a venturi. Time-averaged void fractions were obtained after a detailed image correction and calibration procedure. More information about the cavitation development is extracted using the cross-sectional CT measurements as compared to the high-speed shadowgraphy. We can now quantify the radial geometric features of this complex two-phase flow. The void fraction downstream of the venturi in the bubbly shock mechanism is found to be more than twice compared to the re-entrant jet mechanism. Moreover, the vapor phase mixes with the liquid phase downstream of the venturi, resulting in cloud-like cavitation. This data will be essential to validate our assumptions regarding the physical mechanisms. Furthermore, it will be helpful for the validation of numerical studies.

Using the CT reconstruction, we are able to explore the internal structures of the cavitating flow and to quantify the void fractions. The combination of high-speed shadowgraphy data and CT data gives unprecedented insight into this complex multiphase flow. Despite the new insight that this approach generated, there still is a major limitation: the current study was performed using the time-averaged X-ray measurements; hence, further studies are needed to investigate the transient behavior of the vapor cloud. These investigations are planned and will be performed using phase-locked X-ray measurements.

Acknowledgments

SJ has received funding from Marie Curie Horizon 2020 Research and Innovation programme Grant 642536 'CaFE'. CP has received funding from ERC Consolidator Grant 725183 'OpaqueFlows'. The authors would like to thank Willian Hogendoorn (TU Delft) for providing access to the high-speed shadowgraphy data. The authors further thank Sören Schenke and Amitosh Dash (both TU Delft) for many fruitful discussions.

References

- van Aarle, W., Palenstijn, W.J., Cant, J., Janssens, E., Bleichrodt, F., Dabrvolski, A., De Beenhouwer, J., Batenburg, K.J., Sijbers, J., 2016. Fast and flexible X-ray tomography using the ASTRA toolbox. *Opt. Express* 24 (22), 25129–25147.
- Bauer, D., Barthel, F., Hampel, U., 2018. High-speed X-ray CT imaging of a strongly cavitating nozzle flow. *J. Phys. Commun.* 2 (7), 075009.
- Bauer, D., Chaves, H., Arcoumanis, C., 2012. Measurements of void fraction distribution in cavitating pipe flow using X-ray CT. *Measur. Sci. Technol.* 23 (5), 055302.
- Chaouki, J., Larachi, F., Duduković, M.P., 1997. Noninvasive tomographic and velocimetric monitoring of multiphase flows. *Ind. Eng. Chem. Res.* 36 (11), 4476–4503. doi:10.1021/ie970210t.
- Chen, G.H., Wang, G.Y., Hu, C.L., Huang, B., Zhang, M.D., 2015. Observations and measurements on unsteady cavitating flows using a simultaneous sampling approach. *Exp. Fluids* 56 (2), 32. doi:10.1007/s00348-015-1896-8.
- Dash, A., Jahangir, S., Poelma, C., 2018. Direct comparison of shadowgraphy and X-ray imaging for void fraction determination. *Measur. Sci. Technol.* 29 (12), 125303.
- Duke, D.J., Swantek, A.B., Kastengren, A.L., Powell, C.F., 2015. X-ray diagnostics for cavitating nozzle flow. *J. Phys.* 656 (1), 012110.
- Dular, M., Petkovšek, M., 2015. On the mechanisms of cavitation erosion - coupling high speed videos to damage patterns. *Exp. Thermal Fluid Sci.* 68, 359–370. doi:10.1016/j.expthermflusc.2015.06.001.
- Franc, J.-P., Michel, J.-M., 2006. *Fundamentals of Cavitation*, 76. Springer Science & Business Media.
- Ganesh, H., Mäkiharju, S.A., Ceccio, S.L., 2016. Bubbly shock propagation as a mechanism for sheet-to-cloud transition of partial cavities. *J. Fluid Mech.* 802, 37–78.
- Hayashi, S., Sato, K., 2014. Unsteady behavior of cavitating waterjet in an axisymmetric convergent-Divergent nozzle: high speed observation and image analysis based on frame difference method. *J. Flow Control Measur. Visualizat.* 2, 94–104.
- Helmi, A., Wagner, E., Gallucci, F., van Sint Annaland, M., van Ommen, J., Mudde, R., 2017. On the hydrodynamics of membrane assisted fluidized bed reactors using X-ray analysis. *Chem. Eng. Process.* 122, 508–522. doi:10.1016/j.cep.2017.05.006.
- Holder, D.S., 2004. *Electrical Impedance Tomography: Methods, History and Applications*. CRC Press.
- Jahangir, S., Hogendoorn, W., Poelma, C., 2018. Dynamics of partial cavitation in an axisymmetric converging-diverging nozzle. *Int. J. Multiphase Flow* 106, 34–45. doi:10.1016/j.ijmultiphaseflow.2018.04.019.
- Kastengren, A., Powell, C.F., 2014. Synchrotron X-ray techniques for fluid dynamics. *Exp. Fluids* 55 (3), 1686. doi:10.1007/s00348-014-1686-8.
- Ketcham, R.A., Carlson, W.D., 2001. Acquisition, optimization and interpretation of X-ray computed tomographic imagery: applications to the geosciences. *Comput. Geosci.* 27 (4), 381–400. doi:10.1016/S0098-3004(00)00116-3.
- Khlifa, I., Vabre, A., Hočevar, M., Fezzaa, K., Fuzier, S., Roussette, O., Coutier-Delgosa, O., 2017. Fast X-ray imaging of cavitating flows. *Exp. Fluids* 58 (11), 157.
- Laberteaux, K.R., Ceccio, S.L., Mastrocola, V.J., Lowrance, J.L., 1998. High speed digital imaging of cavitating vortices. *Exp. Fluids* 24 (5), 489–498. doi:10.1007/s003480050198.
- Lee, I.H., Mäkiharju, S.A., Ganesh, H., Ceccio, S.L., 2016. Scaling of gas diffusion into limited partial cavities. *J. Fluid Eng.* 138 (5), 051301.
- Long, X., Zhang, J., Wang, J., Xu, M., Lyu, Q., Ji, B., 2017. Experimental investigation of the global cavitation dynamic behavior in a venturi tube with special emphasis on the cavity length variation. *Int. J. Multiphase Flow* 89, 290–298.
- Mäkiharju, S.A., Gabillet, C., Paik, B.-G., Chang, N.A., Perlin, M., Ceccio, S.L., 2013. Time-resolved two-dimensional X-ray densitometry of a two-phase flow downstream of a ventilated cavity. *Exp. Fluids* 54 (7), 1561. doi:10.1007/s00348-013-1561-z.
- Maurer, S., Wagner, E.C., Schildhauer, T.J., van Ommen, J.R., Biollaz, S.M., Mudde, R.F., 2015. X-Ray measurements of bubble hold-up in fluidized beds with and without vertical internals. *Int. J. Multiphase Flow* 74, 118–124. doi:10.1016/j.ijmultiphaseflow.2015.03.009.
- Mitroglou, N., Lorenzi, M., Santini, M., Gavaises, M., 2016. Application of X-ray micro-computed tomography on high-speed cavitating diesel fuel flows. *Exp. Fluids* 57 (11), 175. doi:10.1007/s00348-016-2256-z.
- Mudde, R.F., Alles, J., van der Hagen, T.H.J.J., 2008. Feasibility study of a time-resolving X-ray tomographic system. *Measur. Sci. Technol.* 19 (8), 085501.
- Peng, C., Tian, S., Li, G., 2018. Joint experiments of cavitation jet: high-speed visualization and erosion test. *Ocean Eng.* 149, 1–13.
- Tomov, P., Khelladi, S., Ravelet, F., Sarraf, C., Bakir, F., Vertenoeuil, P., 2016. Experimental study of aerated cavitation in a horizontal venturi nozzle. *Exp. Thermal Fluid Sci.* 70, 85–95.
- Wang, D., Song, K., Fu, Y., Liu, Y., 2018. Integration of conductivity probe with optical and X-ray imaging systems for local air - water two-phase flow measurement. *Measur. Sci. Technol.* 29 (10), 105301.